




# Tuning Anderson localization of edge-mode graphene plasmons in randomly gated nanoribbons

YINGYING ZHU,<sup>1</sup> CHANG-GUI LI,<sup>1</sup> YI ZHU,<sup>1</sup> BO XIONG,<sup>1</sup> RUWEN PENG,<sup>1,2</sup>  AND MU WANG<sup>1,3</sup>

<sup>1</sup>National Laboratory of Solid State Microstructures, School of Physics, and Collaborative Innovation Center of Advanced Microstructures, Nanjing University, Nanjing 210093, China

<sup>2</sup>rwpeng@nju.edu.cn

<sup>3</sup>muwang@nju.edu.cn

**Abstract:** Edge-mode graphene plasmons (EGPs) supported by graphene nanoribbons are highly confined, and they can show versatile tunability under electrostatic bias. In order to efficiently enhance and actively control the near-field intensity in integrated plasmonic devices, we theoretically study Anderson localization of EGPs in a graphene nanoribbon with an underlying electrode array in this work. By randomly arranging the electrodes in the array, positional disorder is introduced in the graphene nanoribbon system. Consequently, the Anderson localization of EGPs occurs with an exponentially decreased electric field, reduced propagation length, and rapid disappearance of the cross-correlation coefficient. Physically, inhomogeneous gating effectively creates a disordered distribution of Fermi levels in the graphene nanoribbon, which provides adequate fluctuation of the effective refractive index and results in strong localization of the EGPs at mid-infrared regime. By changing electrode array arrangements, the EGPs can be trapped at distinct locations in the nanoribbon. Further considering that the Fermi-level disorder can be introduced by randomly modulating the electrostatic bias, we apply different gate voltages at different electrodes in the array. Electrically tunable Anderson localization of EGPs are eventually realized in those randomly gated nanoribbons. Moreover, by combining both the positional and Fermi-level disorders in the system, the Anderson localization becomes more actively controlled in this electrically gated graphene nanoribbons. It is shown that the local field can be selectively trapped at single distinct location, or even several locations along the graphene nanoribbon. This investigation extends the Anderson localization to the EGPs in the mid-infrared range and enriches the graphene-based active plasmonic devices.

© 2020 Optical Society of America under the terms of the [OSA Open Access Publishing Agreement](#)

## 1. Introduction

Graphene plasmons, which feature the collective excitations of two-dimensional massless electrons, are rapidly emerging as a viable approach for the fast manipulation of light [1,2]. At terahertz and mid-infrared ranges, graphene behaves as a one-atom-thick “metal” that can support highly confined graphene surface plasmons [1–6]. Compared to the surface plasmons in conventional plasmonic materials, such as silver and gold, graphene plasmons possess the following advantageous characters: (i) relatively low dissipative losses, owing to the relatively large conductivity of graphene [4,5]; (ii) extremely small spatial extension compared to the light wavelength, which can stimulate a strong localized optical field and create significantly enhanced light-matter interactions; and (iii) capability of being dynamically tuned via chemical doping [7] or electrostatic gating [8–10]. To further facilitate the field localization of graphene plasmons, various methods have been proposed, such as designing graphene nanostructures [11,12] and introducing plasmonic metasurfaces [13]. The unique optoelectronic properties make graphene

the promising candidate for active plasmonic devices, such as sensors [14,15], modulators [16,17], transformation optical devices [1], integrated photonic circuits [18], and nonlinear devices [19].

Finite-sized graphene geometries, such as graphene nanoribbons, can possess all the advantages noted above and present unique features [20–22]. A graphene nanoribbon can support edge-mode graphene plasmons (EGPs) with the local field concentrated near the boundaries of the nanoribbon. This leads to strong confinement both vertically and laterally, and therefore, allows functions in sensors [23], couplers [24], filters [25] and logic gates [26]. Several approaches have been made to manipulate EGPs, such as altering the shapes or boundaries of the graphene nanostructures [12,27,28], modulating the local dielectric environment [13] and the local doping condition [23,29]. However, further compression of the EGPs in a controlled manner is required specifically in integrated plasmonic devices.

It is well known that Anderson localization, which originates from interference of coherent waves, can significantly confine electromagnetic waves [30–38]. Initially the localization of waves was investigated by Anderson in 1958, which predicts that an electron may become immobile when placed in a disordered lattice [39]. Since then, the Anderson localization has been extensively studied, and it has been extended from an electron to other waves, including matter waves [40], acoustic waves [41], and electromagnetic waves [30–38]. In the optical analogy of Anderson localization, the occurrence of strong localization can be characterized by exponentially decayed local fields [30,33,36], significantly decreased propagation lengths [36] and small correlation coefficients [30]. To date, Anderson localization of light has been successfully observed in optical systems such as disordered photonic lattices [34,35] and coupled waveguide arrays [36], stimulating applications in imaging [42], light harvesting [43,44] and random lasing [45,46]. Recently, using disordered nanogratings, strong localization of surface plasmon polaritons at silver film has been experimentally observed in the visible range [47]. However, the difficulty of altering the permittivity functions of noble metals and the existence of large energy losses at visible wavelengths constrain the efficiency and tunability of plasmonic devices. To circumvent these problems, Anderson localization of graphene plasmons has been proposed [48–50]. Both localized and propagating modes can be trapped in randomly modulated graphene sheets. However, to the best of our knowledge, there have been no prior studies on the Anderson localization of edge-mode plasmons in graphene nanoribbons and its tunability. Naturally it is worthwhile to explore the Anderson localization of edge-mode graphene plasmons (*i.e.*, EGPs).

In this work, we theoretically investigate Anderson localization of EGPs in a graphene nanoribbon with the underlying electrode array. By randomly arranging the electrodes in the array, positional disorder can be introduced in the system. As a result, strong localization of EGPs occurs with an exponentially decreased electric field, reduced propagation length and rapid disappearance of the cross-correlation coefficient. Physically, based on electric-field effect, the disordered electrode array can effectively create desired Fermi-level patterns in a graphene nanoribbon, which provide adequate fluctuation of the effective refractive index. When EGPs propagate along the graphene nanoribbon, some of the waves can tunnel through the randomly gated regions, while others are localized around them. Therefore, Anderson localization of EGPs occurs when the degree of positional disorder is increased. By changing the array arrangements, it is observed that the EGPs can be trapped at distinct positions. Besides, the Fermi-level disorder can be introduced by randomly modulating the electrostatic bias. To achieve this, different gate voltages are applied to different electrode in the array. This configuration leads to the electrically tunable Anderson localization of EGPs. Moreover, when considering the combination of both the positional and Fermi-level disorders, the Anderson localization can be more effectively controlled. Notably, the local electric field can be selectively trapped at one or several distinct positions along the graphene nanoribbon. This study extends the Anderson localization to the EGPs in the mid-infrared range, and provides insight into the active graphene-based plasmonic devices.

## 2. Edge-mode graphene plasmons in a gated graphene nanoribbon

Firstly, we consider the propagating EGPs along a gated graphene nanoribbon. The structure consists of a graphene nanoribbon (of width 150 nm) on top of a silicon substrate with a metallic ground plate, separated by a dielectric spacer layer with refractive index  $n=2$ , as shown in Fig. 1(a). The EGPs (denoted by purple arrows) enter the graphene nanoribbon from the left side and propagate along the  $x$ -direction. Based on the finite-difference time-domain (FDTD) methods, we carried out the numerical simulation on the transportation of the EGPs in the graphene nanoribbon by using a commercial software package (Lumerical, FDTD Solutions). In our simulations, the thickness of the dielectric spacer is set to 400 nm. We use perfectly matched layer (PML) boundary conditions in all directions, and the mesh is set as 0.5 nm in  $x$ - and  $y$ -directions, and 2.5 nm in  $z$ -direction.

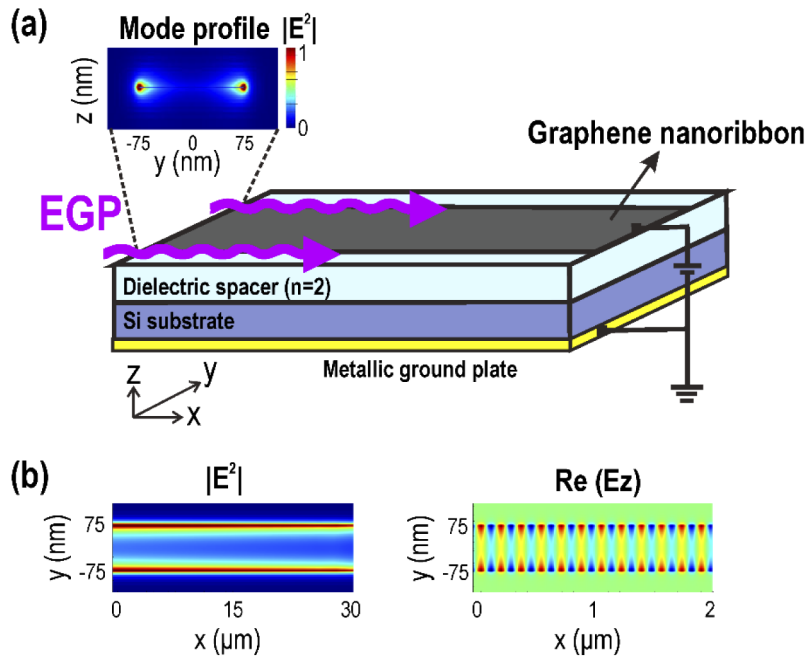


**Fig. 1.** (a) Schematic of a propagating EGP (denoted by purple arrows) in a gated graphene nanoribbon on the substrate. The monolayer graphene nanoribbon has a width of 150 nm and is atop a silicon substrate with a metallic ground plate, separated by a dielectric spacer layer ( $n=2$ ). The Fermi level of the graphene nanoribbon is  $E_{F0}$  and can be tuned through an external electrostatic bias. The left inset shows the electric-field profile of the mode source employed in simulations at  $f=30$  THz, which is calculated using the integrated mode solver in FDTD Solutions. (b) Calculated intensity and the  $z$ -component of the electric field of EGP at  $f=30$  THz, when  $E_{F0}$  is 0.5 eV, plotted in the  $x$ - $y$  plane.

In the simulations performed in this study, the optical conductivity of the monolayer graphene was numerically modeled using Kubo formula. This formalism consists of two parts, *i.e.*, the interband and intraband contributions, in the following equation [51,52]:

$$\sigma(\omega) = \frac{ie^2}{\pi\hbar^2} \frac{E_F}{\omega + i2\Gamma} + \frac{e^2}{4\hbar} \left[ \theta(\hbar\omega - 2E_F) + \frac{i}{\pi} \log \left| \frac{\hbar\omega - 2E_F}{\hbar\omega + 2E_F} \right| \right], \quad (1)$$

where  $\omega$  is the photon frequency in a vacuum,  $E_F$  is the Fermi level of the graphene,  $\Gamma$  is the scattering rate, and  $\theta = (\hbar\omega - 2E_F)$  presents the step function. The scattering rate is assumed to

be  $\Gamma = 0.11$  meV based on the theoretical estimation of the maximum mobility in graphene [53]. When the imaginary part of the graphene conductivity attains positive values in the terahertz and mid-infrared frequencies, the graphene layer effectively behaves as a very thin “metal” layer capable of supporting transverse-magnetic (TM) electromagnetic surface waves. The dispersion relation of the TM-polarized plasmonic waves for the graphene is expressed as [1,54]

$$\beta^2 = k_0^2 [1 - (2/\eta_0\sigma)^2], \quad (2)$$

where  $\beta$  and  $k_0$  are, respectively, the wave vectors in the graphene and free space, and  $\eta_0$  is the intrinsic impedance of the free space. The effective refractive index of the plasmonic mode satisfies  $n_{eff} = \text{Re}(\beta) / k_0$ . Therefore, the optical conductivity of the graphene is strongly dependent of the Fermi level ( $E_F$ ), which can be electrostatically tuned, thus, resulting in dramatic changes in the effective refractive index ( $n_{eff}$ ). This provides a tool for electrically switching the propagation properties of the graphene plasmons.

For graphene nanoribbons, the interdependence between the effective refractive index and the Fermi level of graphene still holds. Previous works have found that graphene nanoribbons can support two types of plasmonic modes, *i.e.* the waveguide mode with the field concentrated along the entire nanoribbon, and the edge mode with the field concentrated near the boundaries of the nanoribbon [20,21]. The latter has even lower propagation losses and higher field confinements. To effectively excite the EGPs in the graphene nanoribbon, the Fermi level of the graphene nanoribbon was set as  $E_{F0} = 0.5$  eV. The TM-polarized EGPs were launched from a mode source located at the left of the simulation space at  $f = 30$  THz, which was calculated using the integrated mode solver in FDTD Solutions. The inset in Fig. 1(a) shows the side-view electric-field distribution of the mode source in the simulations. When the mode source is applied, EGPs are injected in the  $x$ -direction with effective refractive index  $n_{eff} = 54.5 + i0.09$ . This highly compressed mode offers an effective wavelength  $\lambda_{eff} = 182.65$  nm, and a propagation length of  $L = 26.47$   $\mu\text{m}$ . Therefore, the EGPs have a wavelength two orders of magnitude smaller than that of the incident wavelength, and they can propagate several tens of micrometers before being attenuated. Figure 1(b) shows the calculated intensity and  $z$ -component of the electric field in the  $x$ - $y$  plane. It is found that the local field is indeed highly constrained to the rims of the nanoribbon, and it preserves its propagation features after traveling along the entire simulation space. If the Fermi level of graphene is changed to  $E_{F0} = 0.4$  eV and other parameters remain the same,  $n_{eff}$  of the EGPs is changed to  $67.5 + i0.12$ , with an effective wavelength of 147.47 nm and a propagation length of 21.16  $\mu\text{m}$ . The propagation length is further decreased to 10.67  $\mu\text{m}$  when  $E_{F0} = 0.2$  eV. Thus, by altering the Fermi level of graphene, the effective refractive index, and hence the EGP waves in graphene nanoribbons can be modulated.

### 3. Realizing Anderson localization of EGPs with positional disorder

#### 3.1. Structural design, simulation results, and theoretical analysis

Now we try to engineer the EGPs in the graphene nanoribbon by changing the electrode in the system. Instead of using a uniform metallic ground plate, here we place an electrode array underneath the graphene nanoribbon. In this configuration, the electrostatic bias can be spatially varied. As shown in Fig. 2(a), an array of gold parallel bar-electrodes is placed at the bottom of the substrate, and the TM-polarized EGPs are launched on the left side in the  $x$ -direction, while gate voltage  $V_g$  is applied to all the electrodes. It is known that the Fermi level of graphene can be changed using the applied gate voltage ( $V_g$ ) [22]. Therefore, by randomly arranging the electrodes, a disordered gated-stripes array can be created across the graphene nanoribbon. This effectively forms a desired Fermi-level pattern, which provides adequate fluctuation of the effective refractive index ( $n_{eff}$ ), and induces sufficiently strong interference between multiple scattering EGPs. Based on this, the propagation features of EGPs can be affected and Anderson localization of EGPs may occur while increasing the disorder degree.

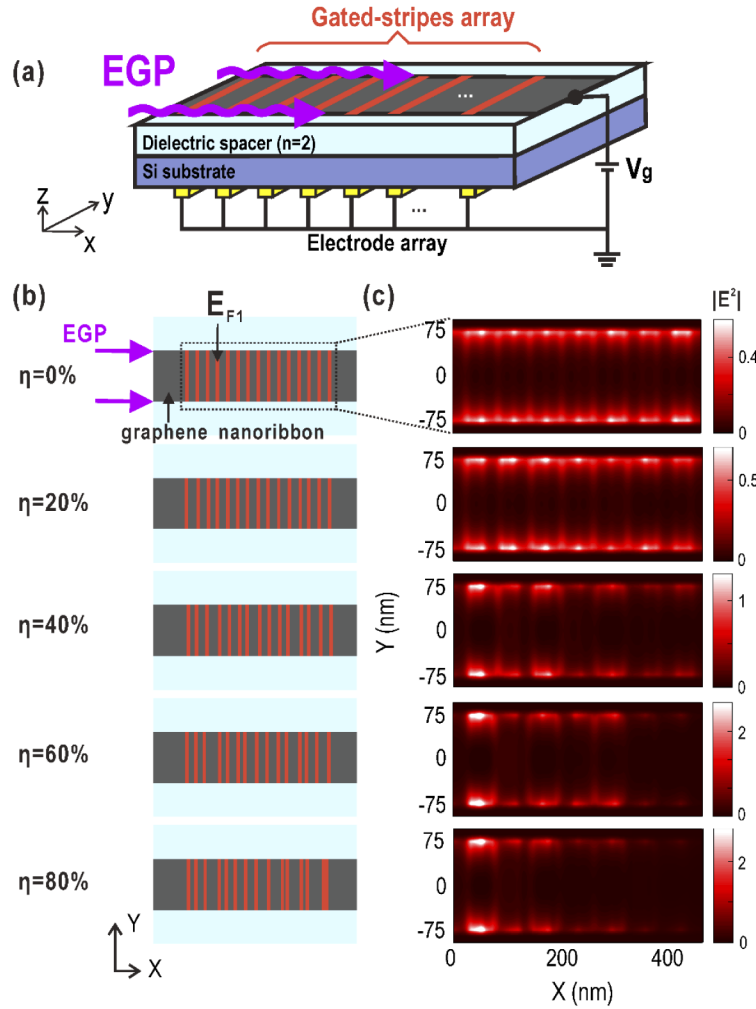


**Fig. 2.** (a) Schematic of a propagating EGP in a graphene nanoribbon, with an array of electrodes at the bottom. Gate voltage  $V_g$  is applied to all electrodes. Therefore, according to the electrode arrangements, an array of gated stripes form a certain Fermi-level pattern across the graphene nanoribbon. (b) Fermi-level patterns across the graphene nanoribbon with different positional disorder degrees, ranging from  $\eta = 0\%$  to  $\eta = 80\%$ , respectively.  $E_{F0}$  ( $E_{F1}$ ) is the Fermi level of graphene segments without (with) the electrodes underneath, denoted by gray (red). The dielectric spacer layer is marked with light blue. Each array pattern consists of 15 stripes, with period  $p = 30$  nm and stripe width  $w = 10$  nm. (c) Calculated electric-field distribution of the EGPs at  $f = 30$  THz. The disorder degree are changed from  $\eta = 0\%$  to  $\eta = 80\%$  corresponding to (b).

The positional disorder degree  $\eta$  is denoted by perturbing the position of each stripe as  $\eta = \Delta x / p$ . Here,  $p$  is the array period and  $\Delta x$  is the random deviation of each stripe from its periodic arrangement. Thus, for a disordered array with  $\eta$ , the position of the  $i^{\text{th}}$  stripe in the array follows  $x_i = ip + \eta p(r - 0.5)$ , where  $r$  is a uniform random number between 0 and 1. The analysis was restricted to an array consisting of 15 stripes. The period and width of the stripes were set to  $p = 30$  nm and  $w = 10$  nm, respectively. The Fermi level of the gated graphene stripes were set to  $E_{F1} = 0.25$  eV, whereas the rest was set to  $E_{F0} = 0.5$  eV, depicted with red and gray colors in

Fig. 2(a). Figure 2(b) shows the Fermi-level patterns with five degrees of  $\eta$ , varying between 0% and 80%.

The calculated field distributions of the EGPs at  $f=30$  THz with different positional disorder degrees are shown in Fig. 2(c). For  $\eta=0\%$ , the EGPs are excited on the edge of the graphene nanoribbon and propagate along the  $x$ -direction. The local field intensity scarcely decreases after travelling along the entire structure. However, when  $\eta$  increases from 20% to 80%, the electric field gradually shrinks, and the propagation length dramatically decreases. Above the threshold of  $\eta=40\%$ , the propagation features of the EGPs almost disappear. Meanwhile, the local field intensity is enhanced owing to the conservation of energy.

To better manifest the localization of the EGPs along the direction of propagation, the field intensity near the boundaries of the nanoribbon was integrated along  $y$  direction. Figure 3(a) shows the integrated field distributions with  $\eta=0\text{--}80\%$ . In the periodic structure ( $\eta=0\%$ ), the frequent oscillations of the localized EGPs can be clearly observed around the gated stripes. The intensity undergoes negligible losses along the entire graphene nanoribbon. On the contrary, when the disorder degree increases, the field exponentially decreases, followed by an enhancement of the local field intensity. Therefore, the Anderson localization of the EGPs occurs in the graphene nanoribbon via modulation of the spatial distribution of the electric field bias.

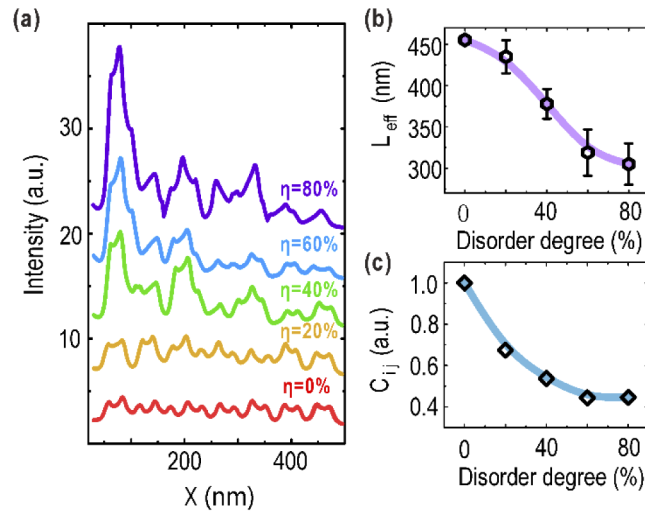


**Fig. 3.** (a) Integrated electric-field intensity along  $y$ -direction near the edge of the nanoribbon at  $f=30$  THz, plotted as a function of  $x$ . The positional disorder degree increased from  $\eta=0\%$  to  $\eta=80\%$ . (b) Calculated effective propagation length  $L_{eff}$  as a function of  $\eta$ , and the values were averaged over 10 structures with different array arrangements. (c) Calculated cross-correlation coefficients  $C_{ij}$  between the periodic structure and disordered structures, plotted as a function of  $\eta$ .

Attempts are then made to quantitatively study the Anderson localization of the EGPs with positional disorder. For each disordered structure, the inverse participation ratio is expressed as [47]

$$P = \frac{\int f^2(x)dx}{\left(\int f(x)dx\right)^2} \quad (3)$$

where  $f(x)$  denotes the electric-field intensity. The effective propagation length  $L_{eff} = \langle 1/P \rangle$  (where  $\langle \dots \rangle$  stands for averaging over multiple structures with different array arrangements) is plotted as a function of the positional disorder degree in Fig. 3(b).  $L_{eff}$  is approximately 460 nm in the periodic structure and decreases to approximately 300 nm when  $\eta=80\%$ . Additionally, it

is known that cross correlation is used to describe the degree of overlap between two different patterns [55]. It provides information about the similarity of the shape regardless of the average intensity of the signals. Here, cross-correlation coefficient  $C_{ij}$  is calculated from [56]

$$C_{ij} = \frac{\text{Cov}(f_i, f_j)}{\sigma_i \sigma_j}, \quad (4)$$

where  $f_i$  and  $f_j$  denote the field distribution of the periodic and disordered structures, respectively. In this equation,  $\text{Cov}(f_i, f_j)$  is the covariance of  $f_i$  and  $f_j$ ; and  $\sigma_i$  and  $\sigma_j$  represent the respective standard deviations of  $f_i$  and  $f_j$ . In general, the normalized cross-correlation coefficient,  $C_{ij}$ , ranges from 0 to 1, and can be interpreted as the degree of overlap between the periodic and disordered structures. The calculated  $C_{ij}$  is shown in Fig. 3(c) as a function of disorder degree. It is found that  $C_{ij}$  equals to 1 when  $\eta = 0\%$ , following which it drops sharply below approximately 0.4 when  $\eta$  surpasses 60% and converges to a constant at a larger disorder degree. As a result, Anderson localization of EGPs indeed appears in the graphene nanoribbon when increasing the positional disorder degree. The strong localization is represented by the exponentially decreased local field, reduced propagation length and rapid disappearance of the cross-correlation coefficient.

### 3.2. Anderson localization in different electrode array arrangements

Naturally we can design different electrode array arrangements under the same positional disorder, and trap the EGPs at different local positions by changing the array arrangements. In Fig. 4(a), three different array arrangements (S1, S2, and S3) are illustrated with the same positional disorder degree  $\eta = 80\%$ , while the other parameters remain unchanged. Figure 4(b) shows the calculated field distribution of EGP waves at  $f = 30$  THz. The calculated cross-correlation coefficient  $C_{ij}$  equals to 0.43, 0.41 and 0.39 for S1, S2 and S3, respectively, manifesting that the Anderson localization emerges in all three structures. However, EGP waves are trapped at different positions. From S1 to S3, respectively, the localized EGPs appear on the left, middle and

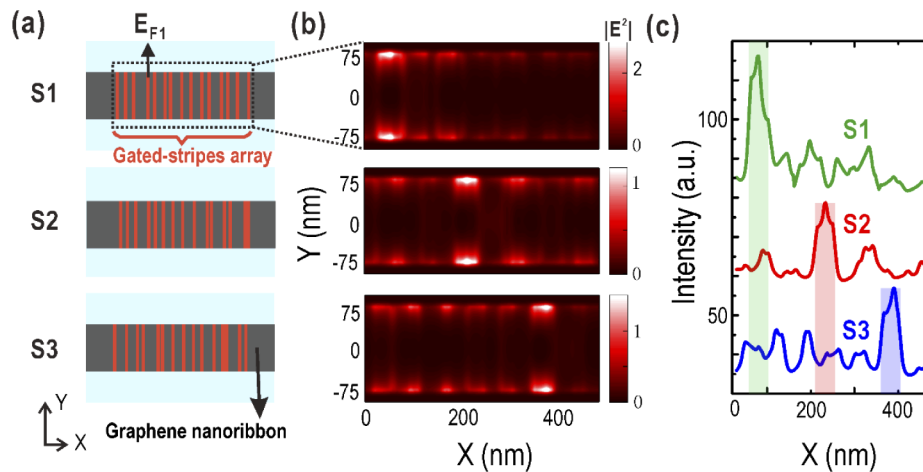


**Fig. 4.** (a) Illustration of the three selected arrangements of the Fermi-level patterns with positional disorder degree  $\eta = 80\%$ , denoted by S1, S2, and S3, respectively.  $E_{F0}$  ( $E_{F1}$ ) is the Fermi level of graphene segments without (with) the underneath electrodes, denoted by gray (red). (b) Calculated electric-field distribution of the EGPs at  $f = 30$  THz, corresponding to the three patterns shown in (a). (c) Integrated electric-field intensity along  $y$ -direction near the edge of the nanoribbon, plotted as a function of  $x$ . The localization positions in S1, S2, S3 are marked with green, red and blue, respectively.

right of the graphene nanoribbon. The integrated field distributions, shown in Fig. 4(c), give a similar but clearer result to that in Fig. 4(b). By fitting the curves in Fig. 4(c) with Gaussian peaks, it is observed that the local field intensity peak at  $x_1 = 77.8$  nm,  $x_2 = 232.6$  nm and  $x_3 = 384.3$  nm for S1, S2, and S3, respectively. Each has a full width at half maximum (FWHM) of 34.7 nm, 37.1 nm, and 34.1 nm, showing similar degrees of localization.

Normally, in disordered metal structures, surface plasmonic waves are localized to the launch site owing to the high energy losses at visible frequencies [46]. However, EGPs undergo relatively low energy losses in the mid-infrared range. Therefore, the localization can occur at entirely different positions along the graphene nanoribbon. These observations imply that the energy can be selectively trapped in the graphene nanoribbon.

#### 4. Tuning Anderson localization of EGPs with Fermi-level disorder

Apart from altering the arrangements of the electrode array, the disorder can also be introduced by randomly modulating the electrostatic bias, or equivalently, the Fermi level of graphene. As shown in Fig. 5(a), based on the periodic array arrangements, different gate voltages  $V_i$  ( $i = 1-n$ ) are applied to different electrodes. Hence, each gated stripe across the graphene nanoribbon has different Fermi energy based on  $V_i$ , as depicted by the color scale from white to red in Fig. 5(a). Similarly, the propagating EGPs along the graphene nanoribbon can sense the

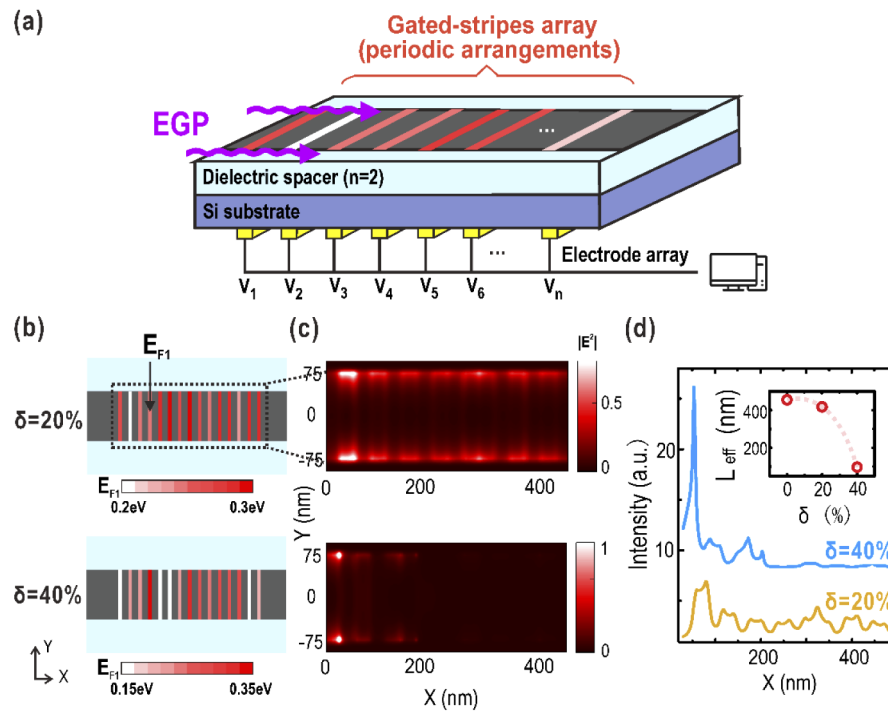


**Fig. 5.** (a) Schematic of a propagating EGP in a graphene nanoribbon with a periodic array of electrodes at the bottom. Different gate voltages, varying from  $V_1$  to  $V_n$  are applied to each electrode. (b) Fermi-level patterns across the graphene nanoribbon with Fermi-level disorder degree  $\delta = 20\%$  and  $40\%$ . The Fermi level of the gated graphene stripes  $E_{F1}$  are depicted by the color scale from white to red. (c) Calculated electric-field distribution of the EGPs at  $f = 30$  THz, corresponding to the patterns shown in (b). (d) Integrated electric-field intensity along  $y$ -direction near the edge of the nanoribbon, plotted as a function of  $x$ . Inset is the effective propagation length  $L_{eff}$ , as the function of Fermi-level disorder degree.



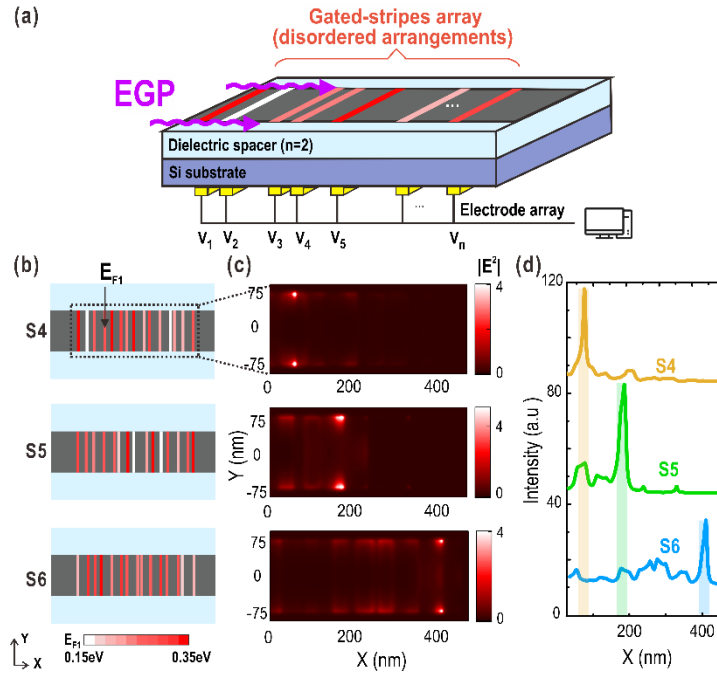
disordered fluctuation of the effective refractive index, resulting in the occurrence of actively controllable Anderson localization. Here, the Fermi-level disorder degree is defined as  $\delta = \Delta E_{F1} / E_{\text{const}}$ , where  $E_{\text{const}}$  is set to a constant 0.25 eV. This indicates that the Fermi level of each gated graphene stripe ( $E_{F1}$ ) has a random deviation  $\Delta E_{F1}$  from  $E_{\text{const}}$ .

Figure 5(b) illustrates the Fermi-level patterns with  $\delta = 20\%$  and  $40\%$ .  $E_{F1}$  ranges from 0.2 eV to 0.3 eV for  $\delta = 20\%$ , and from 0.15 eV to 0.35 eV for  $\delta = 40\%$ , depicted by the color scale from white to red in Fig. 5(b). Figure 5(c) shows the calculated field distribution of EGPs at  $f = 30$  THz along the  $x$ -direction. Notably, the Anderson localization occurs when increasing the Fermi-level disorder. The integrated electric-field distributions of the two structures,  $\delta = 20\%$  and  $40\%$ , are plotted using yellow and blue in Fig. 5(d). It is seen that when the Fermi-level disorder increases, the EGP modes are highly compressed, followed by an exponential decreased in the field, remarkable enhancement in the local field intensity and relatively small cross-correlation coefficient  $C_{ij}$  (calculated as 0.25 when  $\delta = 40\%$ ). The inset in Fig. 5(d) shows the effective propagation length,  $L_{\text{eff}}$ , as a function of Fermi-level disorder.  $L_{\text{eff}}$  rapidly drops below 90 nm when  $\delta$  increases to  $40\%$ , approximately one third of the value obtained from the passive strategy used in the previous section. Thus, the Anderson localization of EGPs is successfully realized in the gated graphene nanoribbon by electrostatically introducing the Fermi-level disorder.

## 5. Tuning Anderson localization of EGPs with both positional and Fermi-level disorders

Now we are ready to combine both the positional and Fermi-level disorders, and try to control more effectively the Anderson localization of the EGPs in the electrically gated graphene nanoribbons. As illustrated in Fig. 6(a), the position and applied gate voltage of each electrode in the array can be altered simultaneously. Three different patterns of the Fermi level, denoted by S4, S5, and S6, respectively, are shown in Fig. 6(b). Each has a positional disorder degree of  $\eta = 80\%$ , and Fermi-level disorder degree of  $\delta = 40\%$ , while the other parameters remain unchanged. Figure 6(c) shows the calculated field distribution of the EGPs at  $f = 30$  THz. Here, the relatively small value of calculated cross-correlation coefficient  $C_{ij}$  in S4–S6 (equals to 0.15, 0.13 and 0.24 for S4, S5 and S6, respectively) verify that the occurrence of the Anderson localization of EGPs. In Fig. 6(c), from S4 to S6, the EGPs are found to be localized at on the left, middle, and right of the graphene nanoribbon, respectively. Compared to S1–S3 in Fig. 4, the local field intensity of S4–S6 are more enhanced and localized. In Fig. 6(d), the integrated field distributions show the local field intensity peak at  $x_4 = 67.1$  nm,  $x_5 = 174.8$  nm and  $x_6 = 410.2$  nm along the  $x$ -direction in S4, S5 and S6, respectively. The calculated FWHM is 11.8 nm, 21.6 nm and 16.6 nm, respectively, almost half of the S1–S3 values. The decrease of the FWHM indicates that the EGPs are further localized when combining the two types of disorder.

Moreover, by tuning the position and applied gate voltage of each electrode in the electrode array, the EGPs can be trapped at several different positions in the same graphene nanoribbon. Figure 7(a) illustrates two arrangements of the Fermi level, S7 and S8, using the same parameters as in Fig. 6(a). Both have positional disorder degree  $\eta = 80\%$  and Fermi-level disorder degree  $\delta = 40\%$ . The calculated field distribution and integrated field intensities, respectively, of EGPs at  $f = 30$  THz are plotted in Figs. 7(b) and (c). Strong localization appears with the calculated cross-correlation coefficient  $C_{ij}$  of 0.23 and 0.26 for S7 and S8, respectively. Additionally, it can be seen that the EGPs are localized at two (three) distinct positions in S7 (S8). In S7, the local field peaks at  $x_7 = 55.2$  nm and 182.3 nm, with the FWHM of 13.3 nm and 26.9 nm. In S8, the local field peaks at  $x_8 = 53.8$  nm, 260.5 nm and 327.9 nm, with the FWHM of 30.1 nm, 28.3 nm and 22.2 nm. These results imply that energy can be in-plane selectively trapped at single or multiple positions. This offers more possibilities for controlled light trapping. Thus, it is clear that by combining both the positional and Fermi-level disorders, the Anderson localization of EGPs in the gated graphene nanoribbon can be more effectively controlled and functionalized.



**Fig. 6.** (a) Schematic of a propagating EGP in a graphene nanoribbon, with a disordered array of electrode at the bottom. The positions and applied voltages of each electrode are controlled independently. The gate voltage is varied from  $V_1$  to  $V_n$ . (b) Three Fermi-level patterns, denoted by S4, S5, and S6, respectively, with positional disorder degree  $\eta = 80\%$  and Fermi-level disorder degree  $\delta = 40\%$ . (c) Calculated electric-field distribution of the EGPs at  $f = 30$  THz, corresponding to the patterns shown in (b). (d) Integrated electric-field intensity along  $y$ -direction near the edge of the nanoribbon, plotted as a function of  $x$ . The localization positions in S4, S5, S6 are marked with yellow, green and blue respectively.

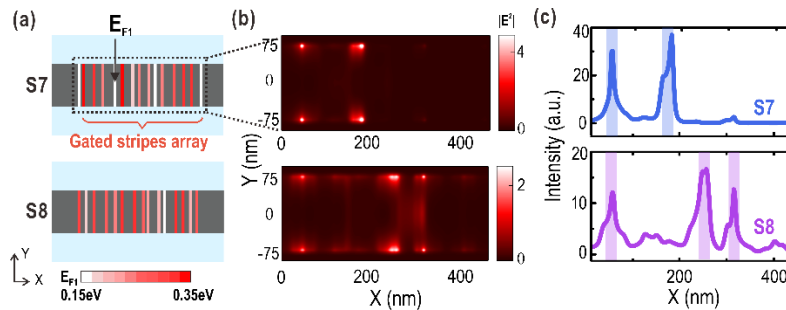


**Fig. 7.** (a) Fermi-level patterns across the graphene nanoribbon with  $\eta = 80\%$  and  $\delta = 40\%$ , denoted with S7 and S8. The Fermi level of the gated graphene stripes  $E_{F1}$  are depicted by different colors, from white to red. (b) Calculated electric-field distribution of the EGPs at  $f = 30$  THz, corresponding to the patterns shown in (a). (c) Integrated electric-field intensity along  $y$ -direction near the edge of the nanoribbon, plotted as a function of  $x$ . The localization positions in S7 and S8 are marked with blue and purple.

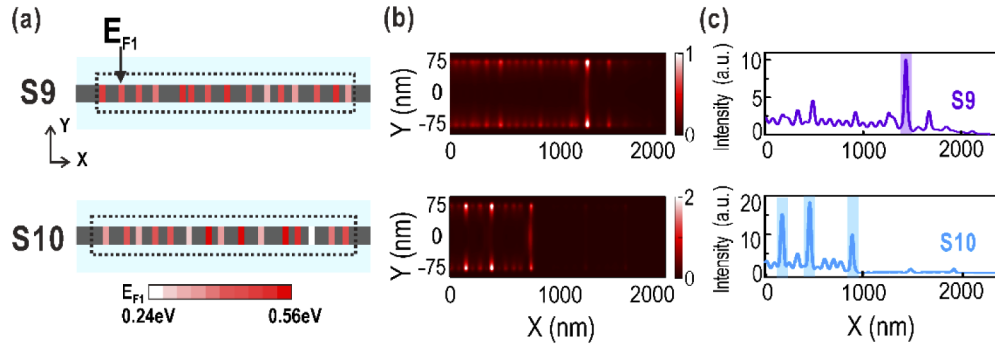


**Fig. 8.** (a) Fermi-level patterns across the graphene nanoribbon with positional disorder degree  $\eta = 80\%$  and Fermi-level disorder degree  $\delta = 40\%$ , denoted with S9 and S10. The Fermi level of the gated graphene stripes  $E_{F1}$  are depicted by different colors, from white to red. (b) Calculated electric-field distribution of the EGPs at  $f = 30$  THz, corresponding to the patterns shown in (a). (c) Integrated electric-field intensity along  $y$ -direction near the edge of the nanoribbon, plotted as a function of  $x$ . S9, S10 and their localization positions are marked with purple and blue.

It is worthwhile to mention that the relatively small dimension of the graphene stripes (width of 10 nm) may cause quantum effects, and doping of the graphene under such dimension may be challenging if we concern real-world fabrication. To match the present dimensions of the devices which are practically achievable in experiments [57,58], here we enlarge the period and width of the gated-stripes array to  $p = 150$  nm and  $w = 50$  nm, respectively, while the other geometric parameters remain unchanged. The Fermi level of graphene was set to  $E_{F0} = 0.6$  eV, and  $E_{\text{const}}$  was set to 0.4 eV. In Fig. 8(a), we show two Fermi-level patterns S9 and S10 with positional disorder degree  $\eta = 80\%$  and Fermi-level disorder degree  $\delta = 40\%$ . The calculated field distributions and integrated field intensities, respectively, of EGPs at  $f = 30$  THz are plotted in Figs. 8(b) and (c). Strong localization of EGPs are observed with the calculated cross-correlation coefficient  $C_{ij}$  of 0.30 and 0.34 for S9 and S10, respectively. In S9, the EGPs are localized at  $x_9 = 1436.1$  nm with FWHM of 18.2 nm. In S10, the EGPs are localized at  $x_{10} = 192.6$  nm, 471.6 nm and 902.7 nm, with FWHM of 16.3 nm, 16.1 nm and 17.2 nm, respectively. Thus, it is possible to realize the tunable Anderson localization of EGPs when enlarging the size of the gated-stripes array.

## 6. Conclusions

In this work, the Anderson localization of EGPs has been numerically studied along a graphene nanoribbon with an underlying electrode array in the mid-infrared range. By randomly arranging the electrodes in the array, we successfully introduce positional disorder in the system. As a result, the Anderson localization of the EGPs occurs with the exponentially decreased electric field, reduced propagation length, and rapid disappearance of the cross-correlation coefficient. Physically, the inhomogeneous gating provides adequate fluctuation of the effective refractive index. The superposition of multiple EGPs generated by the disorder leads to the Anderson localization of the EGPs. In different array arrangements, it is observed that the EGPs can be trapped at distinct positions owing to their low energy losses. Besides, Fermi-level disorder can be introduced by randomly modulating the electrostatic bias. To achieve this, different gate voltages are applied to different electrodes in the array. Hence, electrically tunable Anderson localization of the EGPs occurs. Moreover, by combining both the positional and Fermi-level disorders, the Anderson localization of the EGPs can be more effectively controlled in this randomly gated graphene nanoribbon. It is shown that local near-field intensity can be selectively

trapped at one or several distinct positions. The theoretical study of the Anderson localization of EGPs herein suggests that graphene can be a low-loss one-atom-thick platform for active plasmonic applications, and it could stimulate tunable light trapping and controllable light-matter interactions.

## Funding

National Key Research and Development Program of China (2017YFA0303702); National Natural Science Foundation of China (11634005, 11674155, 11974177, 61975078).

## Disclosures

The authors declare no conflicts of interest.

## References

1. A. Vakil and N. Engheta, "Transformation optics using graphene," *Science* **332**(6035), 1291–1294 (2011).
2. A. N. Grigorenko, M. Polini, and K. S. Novoselov, "Graphene plasmonics," *Nat. Photonics* **6**(11), 749–758 (2012).
3. T. Low and P. Avouris, "Graphene plasmonics for terahertz to mid-infrared applications," *ACS Nano* **8**(2), 1086–1101 (2014).
4. Q. Bao and K. P. Loh, "Graphene photonics, plasmonics, and broadband optoelectronic devices," *ACS Nano* **6**(5), 3677–3694 (2012).
5. Y. Bao, S. Zu, Y. Zhang, and Z. Fang, "Active control of graphene-based unidirectional surface plasmon launcher," *ACS Photonics* **2**(8), 1135–1140 (2015).
6. Y. Zhou, Y.-Y. Zhu, K. Zhang, H.-W. Wu, R.-W. Peng, R.-H. Fan, and M. Wang, "Plasmonic band structures in doped graphene tubes," *Opt. Express* **25**(11), 12081–12089 (2017).
7. P. Mulvaney, J. Pérez-Juste, M. Giersig, L. M. Liz-Marzán, and C. Pecharromán, "Drastic surface plasmon mode shifts in gold nanorods due to electron charging," *Plasmonics* **1**(1), 61–66 (2006).
8. J. Chen, M. Badioli, P. Alonso-González, S. Thongrattanasiri, F. Huth, J. Osmond, M. Spasenović, A. Centeno, A. Pesquera, P. Godignon, A. Zurutuza Elorza, N. Camara, F. J. G. de Abajo, R. Hillenbrand, and F. H. L. Koppens, "Optical nano-imaging of gate-tunable graphene plasmons," *Nature* **487**(7405), 77–81 (2012).
9. W. Gao, G. Shi, Z. Jin, J. Shu, Q. Zhang, R. Vajtai, P. M. Ajayan, J. Kono, and Q. Xu, "Excitation and active control of propagating surface plasmon polaritons in graphene," *Nano Lett.* **13**(8), 3698–3702 (2013).
10. F.-Z. Shu, R.-H. Fan, J.-N. Wang, R.-W. Peng, and M. Wang, "Advances in dynamically tunable plasmonic materials and devices," *Acta Phys. Sin.* **68**(14), 147303 (2019).
11. Z. Fang, S. Thongrattanasiri, A. Schlather, Z. Liu, L. Ma, Y. Wang, P. M. Ajayan, P. Nordlander, N. J. Halas, and F. J. García de Abajo, "Gated tunability and hybridization of localized plasmons in nanostructured graphene," *ACS Nano* **7**(3), 2388–2395 (2013).
12. S.-X. Xia, X. Zhai, L.-L. Wang, Q. Lin, and S.-C. Wen, "Localized plasmonic field enhancement in shaped graphene nanoribbons," *Opt. Express* **24**(15), 16336–16348 (2016).
13. S.-X. Xia, X. Zhai, Y. Huang, J.-Q. Liu, L.-L. Wang, and S.-C. Wen, "Graphene surface plasmons with dielectric metasurfaces," *J. Lightwave Technol.* **35**(20), 4553–4558 (2017).
14. L. Wu, H. Chu, W. Koh, and E. Li, "Highly sensitive graphene biosensors based on surface plasmon resonance," *Opt. Express* **18**(14), 14395–14400 (2010).
15. W. Xu, L. Xie, J. Zhu, L. Tang, R. Singh, C. Wang, Y. Ma, H.-T. Chen, and Y. Ying, "Terahertz biosensing with a graphene-metamaterial heterostructure platform," *Carbon* **141**, 247–252 (2019).
16. D. Ansell, I. P. Radko, Z. Han, F. J. Rodriguez, S. I. Bozhevolnyi, and A. N. Grigorenko, "Hybrid graphene plasmonic waveguide modulators," *Nat. Commun.* **6**(1), 8846 (2015).
17. H. Qian, Y. Ma, Q. Yang, B. Chen, Y. Liu, X. Guo, S. Lin, J. Ruan, X. Liu, and L. Tong, "Electrical tuning of surface plasmon polariton propagation in graphene–nanowire hybrid structure," *ACS Nano* **8**(3), 2584–2589 (2014).
18. J. T. Kim and S.-Y. Choi, "Graphene-based plasmonic waveguides for photonic integrated circuits," *Opt. Express* **19**(24), 24557–24562 (2011).
19. C. Lu, X. Hu, F. Zhang, H. Yang, and Q. Gong, "Multilayer graphene: polycrystalline ITO for ultralow-power active control of polarization-insensitive, metamaterial-induced transparency," *Adv. Opt. Mater.* **2**(12), 1141–1148 (2014).
20. A. Y. Nikitin, F. Guinea, F. García-Vidal, and L. Martín-Moreno, "Edge and waveguide terahertz surface plasmon modes in graphene microribbons," *Phys. Rev. B* **84**(16), 161407 (2011).
21. J. Christensen, A. Manjavacas, S. Thongrattanasiri, F. H. Koppens, and F. J. García de Abajo, "Graphene plasmon waveguiding and hybridization in individual and paired nanoribbons," *ACS Nano* **6**(1), 431–440 (2012).
22. M. Janfaza, M. A. Mansouri-Birjandi, and A. Tavousi, "Proposal for a graphene nanoribbon assisted mid-infrared band-stop/band-pass filter based on Bragg gratings," *Opt. Commun.* **440**, 75–82 (2019).
23. Y. Li, Y. Su, Q. Lin, X. Zhai, and L.-L. Wang, "Active control of an edge-mode-based plasmon-induced absorption sensor," *Appl. Opt.* **57**(10), 2698–2703 (2018).

24. J. Wang, W. B. Lu, X. B. Li, Z. H. Ni, and T. Qiu, "Graphene plasmon guided along a nanoribbon coupled with a nanoring," *J. Phys. D: Appl. Phys.* **47**(13), 135106 (2014).
25. B. Zhu, G. Ren, Y. Gao, Y. Yang, B. Wu, Y. Lian, J. Wang, and S. Jian, "Spatial splitting and coupling of the edge modes in the graphene bend waveguide," *Plasmonics* **10**(3), 745–751 (2015).
26. X. B. Li, W. B. Lu, J. Wang, J. Hu, Z. G. Liu, B. H. Huang, and H. Chen, "Edge mode graphene plasmons based all-optical logic gates," *Photonics Nanostruct. Fundam. Appl.* **33**, 66–69 (2019).
27. X. Zhu, W. Yan, N. A. Mortensen, and S. Xiao, "Bends and splitters in graphene nanoribbon waveguides," *Opt. Express* **21**(3), 3486–3491 (2013).
28. S. He, X. Zhang, and Y. He, "Graphene nano-ribbon waveguides of record-small mode area and ultra-high effective refractive indices for future VLSI," *Opt. Express* **21**(25), 30664–30673 (2013).
29. D. L. Sounas and C. Caloz, "Edge surface modes in magnetically biased chemically doped graphene nanoribbons," *Appl. Phys. Lett.* **99**(23), 231902 (2011).
30. M. Segev, Y. Silberberg, and D. N. Christodoulides, "Anderson localization of light," *Nat. Photonics* **7**(3), 197–204 (2013).
31. D. S. Wiersma, P. Bartolini, A. Lagendijk, and R. Righini, "Localization of light in a disordered medium," *Nature* **390**(6661), 671–673 (1997).
32. M. Störzer, P. Gross, C. M. Aegerter, and G. Maret, "Observation of the critical regime near Anderson localization of light," *Phys. Rev. Lett.* **96**(6), 063904 (2006).
33. Y. Lahini, A. Avidan, F. Pozzi, M. Sorel, R. Morandotti, D. N. Christodoulides, and Y. Silberberg, "Anderson localization and nonlinearity in one-dimensional disordered photonic lattices," *Phys. Rev. Lett.* **100**(1), 013906 (2008).
34. C. Zhong, C. Wang, and F. Lu, "Localization of light in induced triangular photonic lattices with defects," *Phys. Lett. A* **381**(31), 2544–2549 (2017).
35. T. Schwartz, G. Bartal, S. Fishman, and M. Segev, "Transport and Anderson localization in disordered two-dimensional photonic lattices," *Nature* **446**(7131), 52–55 (2007).
36. L. Martin, G. Di Giuseppe, A. Perez-Leija, R. Keil, F. Dreisow, M. Heinrich, S. Nolte, A. Szameit, A. F. Abouraddy, D. N. Christodoulides, and B. E. A. Saleh, "Anderson localization in optical waveguide arrays with off-diagonal coupling disorder," *Opt. Express* **19**(14), 13636–13646 (2011).
37. A. Ghadi, S. Nouri Jouybari, and M.-R. Panjehpour, "Diffraction engineering Anderson localization of light in nonlinear waveguide array with Kerr and two photon absorption effects," *J. Mod. Opt.* **64**(13), 1247–1256 (2017).
38. L. Dal Negro, C. J. Oton, Z. Gaburro, L. Pavesi, P. Johnson, A. Lagendijk, R. Righini, M. Colocci, and D. S. Wiersma, "Light transport through the band-edge states of Fibonacci quasicrystals," *Phys. Rev. Lett.* **90**(5), 055501 (2003).
39. P. W. Anderson, "Absence of diffusion in certain random lattices," *Phys. Rev.* **109**(5), 1492–1505 (1958).
40. J. Billy, V. Josse, Z. Zuo, A. Bernard, B. Hambrecht, P. Lugan, D. Clément, L. Sanchez-Palencia, P. Bouyer, and A. Aspect, "Direct observation of Anderson localization of matter waves in a controlled disorder," *Nature* **453**(7197), 891–894 (2008).
41. H. Hu, A. Strybulevych, J. Page, S. E. Skipetrov, and B. A. van Tiggelen, "Localization of ultrasound in a three-dimensional elastic network," *Nat. Phys.* **4**(12), 945–948 (2008).
42. S. Karbasi, R. J. Frazier, K. W. Koch, T. Hawkins, J. Ballato, and A. Mafi, "Image transport through a disordered optical fibre mediated by transverse Anderson localization," *Nat. Commun.* **5**(1), 3362 (2014).
43. M. Aeschlimann, T. Brixner, D. Differt, U. Heinzmann, M. Hensen, C. Kramer, F. Lükermann, P. Melchior, W. Pfeiffer, M. Piecuch, C. Schneider, H. Stiebig, C. Strüber, and P. Thielen, "Perfect absorption in nanotextured thin films via Anderson-localized photon modes," *Nat. Photonics* **9**(10), 663–668 (2015).
44. N. J. Hogan, A. S. Urban, C. Ayala-Orozco, A. Pimpinelli, P. Nordlander, and N. J. Halas, "Nanoparticles heat through light localization," *Nano Lett.* **14**(8), 4640–4645 (2014).
45. J. Liu, P. D. Garcia, S. Ek, N. Gregersen, T. Suhr, M. Schubert, J. Mork, S. Stobbe, and P. Lodahl, "Random nanolasing in the Anderson localized regime," *Nat. Nanotechnol.* **9**(4), 285–289 (2014).
46. B. Abaie, E. Mobini, S. Karbasi, T. Hawkins, J. Ballato, and A. Mafi, "Random lasing in an Anderson localizing optical fiber," *Light: Sci. Appl.* **6**(8), e17041 (2017).
47. W.-B. Shi, L.-Z. Liu, R. Peng, D.-H. Xu, K. Zhang, H. Jing, R.-H. Fan, X.-R. Huang, Q.-J. Wang, and M. Wang, "Strong localization of surface plasmon polaritons with engineered disorder," *Nano Lett.* **18**(3), 1896–1902 (2018).
48. Y. Xu and H.-D. Deng, "Tunable Anderson localization in disordered graphene sheet arrays," *Opt. Lett.* **41**(3), 567–570 (2016).
49. M. Sani, M. H. Farzad, A. Hatef, and F. Safarzadeh, "Tunable Anderson localization of propagating graphene surface plasmon modes in a random modulated graphene monolayer," *Europhys. Lett.* **122**(6), 67004 (2018).
50. M. Sani and M. H. Farzad, "Anderson localization of surface plasmons in monolayer graphene," *Phys. Rev. B* **97**(8), 085406 (2018).
51. H. Lu, C. Zeng, Q. Zhang, X. Liu, M. M. Hossain, P. Reineck, and M. Gu, "Graphene-based active slow surface plasmon polaritons," *Sci. Rep.* **5**(1), 8443 (2015).
52. F. J. Garcia de Abajo, "Graphene plasmonics: challenges and opportunities," *ACS Photonics* **1**(3), 135–152 (2014).
53. G. W. Hanson, "Dyadic Green's functions and guided surface waves for a surface conductivity model of graphene," *J. Appl. Phys.* **103**(6), 064302 (2008).

54. W. Gao, J. Shu, C. Qiu, and Q. Xu, "Excitation of plasmonic waves in graphene by guided-mode resonances," *ACS Nano* **6**(9), 7806–7813 (2012).
55. N. Murphy, R. Wortis, and W. Atkinson, "Generalized inverse participation ratio as a possible measure of localization for interacting systems," *Phys. Rev. B* **83**(18), 184206 (2011).
56. E. Manders, F. Verbeek, and J. Aten, "Measurement of co-localization of objects in dual-colour confocal images," *J. Microsc.* **169**(3), 375–382 (1993).
57. C. Santschi, M. Jenke, P. Hoffmann, and J. Brugger, "Interdigitated 50 nm Ti electrode arrays fabricated using XeF<sub>2</sub> enhanced focused ion beam etching," *Nanotechnology* **17**(11), 2722–2729 (2006).
58. S. Partel, C. Dincer, S. Kasemann, J. Kieninger, J. Edlinger, and G. Urban, "Lift-off free fabrication approach for periodic structures with tunable nano gaps for interdigitated electrode arrays," *ACS Nano* **10**(1), 1086–1092 (2016).